



Very Local Impact on the Spectrum of Cosmic-Ray Nuclei below 100 TeV

M.A. Malkov^{a,*}, I.V. Moskalenko^b, P.H. Diamond^a, M. Cao^a

^aDepartment of Astronomy and Astrophysics, University of California San Diego, La Jolla, CA 92093, USA

^bHansen Experimental Physics Laboratory and Kavli Institute for Particle Astrophysics and Cosmology, Stanford University, Stanford, CA 94305, USA

Received June 18, 2024;

Abstract

Recent measurements of primary and secondary CR spectra, their arrival directions, and our improved knowledge of the magnetic field geometry around the heliosphere allow us to set a bound on the distance beyond which a puzzling 10-TeV “bump” and certain related spectral features *cannot* originate. The sharpness of the spectral breaks associated with the bump, the abrupt change of the CR intensity across the local magnetic equator (90° pitch angle), and the similarity between the primary and secondary CR spectral patterns point to a local reacceleration of the bump particles out of the background CRs. We argue that, owing to a steep preexisting CR spectrum, a nearby shock may generate such a bump by boosting particle rigidity by a mere factor of ~ 1.5 in the range below 50 TV. Reaccelerated particles below ~ 0.5 TV are convected with the interstellar medium flow and do not reach the Sun. The particles above this rigidity then form the bump. This single universal process is responsible for the observed spectral features of all CR nuclei, primary and secondary, in the rigidity range below 100 TV. We propose that one viable candidate is the system of shocks associated with ϵ Eridani star at 3.2 pc of the Sun, which is well aligned with the direction of the local magnetic field. Other shocks, such as old supernova shells, may produce a similar effect. We provide a simple formula that reproduces the spectra of all CR species with only three parameters uniquely derived from the CR proton data. We show how our formalism predicts helium, boron, carbon, oxygen, and iron spectra. Our model thus unifies all the CR spectral features observed below 50 TV.

© 2024 COSPAR. Published by Elsevier Ltd All rights reserved.

cosmic rays, propagation, shock wave; bow shock; anisotropy; epsilon Eridani star

1. Introduction

Sources of cosmic rays (CRs) are scattered across the *Galaxy*. After propagation to the Earth, accompanied by a turbulent reacceleration in stochastic magnetic fields and a partial leak into intergalactic space, CRs are expected to arrive with a featureless power-law energy spectrum. The angular distribution should be weakly anisotropic with a dipolar component $\sim 10^{-3}$, indicating that more particles come from the *inner Galaxy* (Secs.2.2 and 4.3). However, the new observations revealed a prominent structure in the *spectra of CR primaries* (so-called 10-TeV “bump”) also characterized by an *excess pointing to the outer Galaxy* with a sharp step-like boundary in CR arrival directions and similar spectral

anomalies in secondary CR *species*.

Understanding the origin of the bump offers a deeper insight into the nature of CR propagation from their sources, individual source contributions to the CR spectrum, and the structure of the local *interstellar medium (ISM)*. Upon addressing the new challenges, we can test and improve the concept of CR origin and guide future observations.

This paper focuses on CR *reacceleration and propagation in the local ISM* (~ 10 pc of the Sun). An exceptional sharpness of the breaks in the *spectra of CR species* resolved by AMS-02, CALET, DAMPE, and ISS-CREAM orbital instruments, dictates this choice. *These features persist within unprecedentedly tight error bounds*. Local SNRs at the distances of 100s pc are unlikely responsible for these structures. Propagating CRs from *such sources* would erase fine spectral features, such as sharp breaks in rigidity spectra

*Corresponding author: mmalkov@ucsd.edu

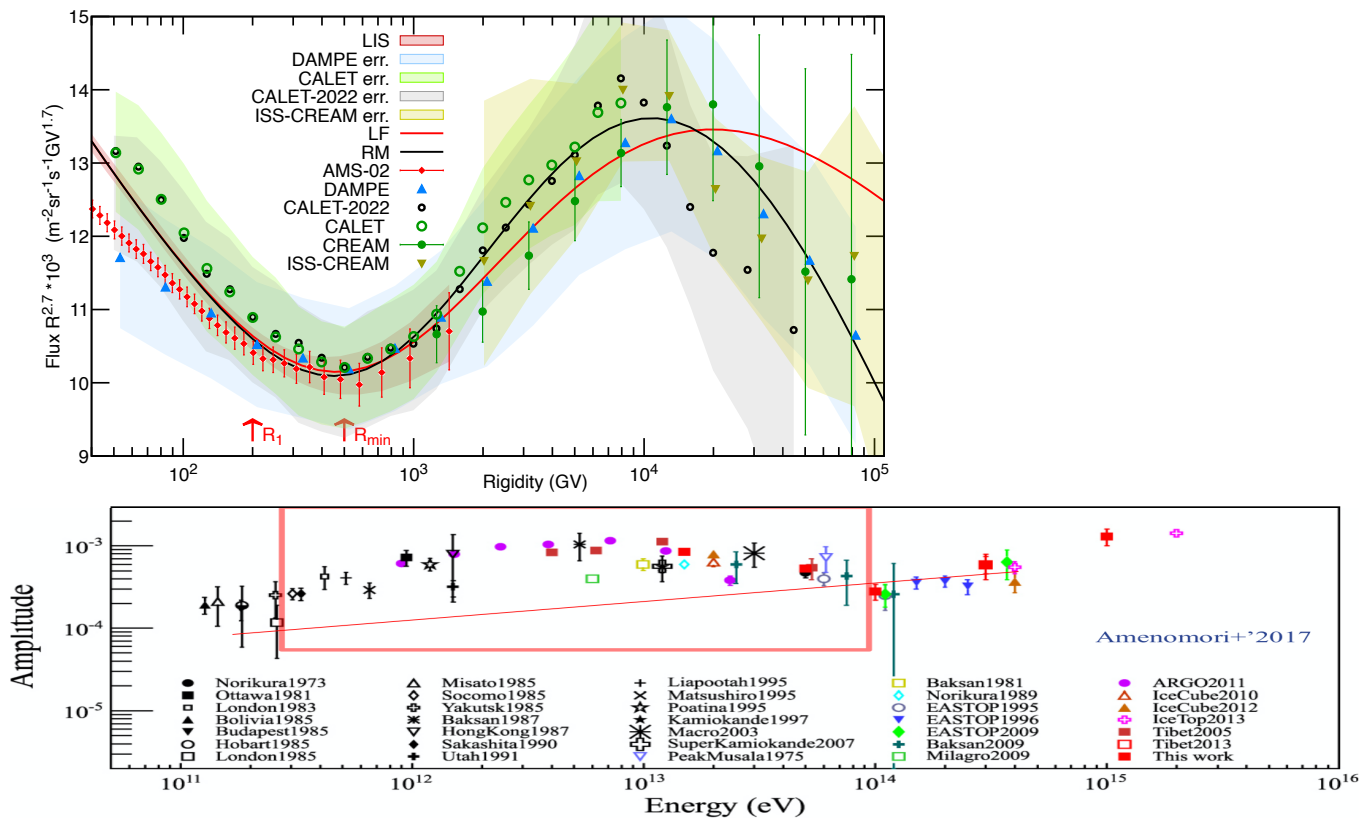


Fig. 1. **Top**: New prominent spectral features, shown in the 10^2 – 10^5 GV range for protons. Compilation of data from AMS-02 (Aguilar et al. 2021a), CALET (Adriani et al. 2019, 2022b), CREAM (Yoon et al. 2017), ISS-CREAM (Choi et al. 2022), and DAMPE (An et al. 2019) is described in Sec. 2. An arrow labeled R_1 shows the break rigidity. Note that the shown CALET, DAMPE, and ISS-CREAM data are adjusted to match the ISM spectrum (Boschini et al. 2020) at the minimum at $R_{min} \approx 500$ GV. This requires shifts in both the rigidity and normalization, which are individual for each set of data. In particular, the older CALET (Adriani et al. 2019) and DAMPE data points are shifted as described in Malkov & Moskalenko (2022). The adjustments used for the older CALET data are also applied to the newer CALET data set (Adriani et al. 2022b). The CREAM and ISS-CREAM data points are renormalized by a factor of 1.12 to match the CALET data (Adriani et al. 2022b). The local interstellar spectrum (LIS) is taken from Boschini et al. (2020), where the marked uncertainty corresponds to the uncertainty in the AMS-02 data. The lines show the local ISM spectra in two models, Eq. (1): *Red* – without CR losses from the magnetic flux tube, *Black* – the same fit with losses (Tables 1 and 2). **Bottom**: CR anisotropy data with the energy scale aligned with the top panel, adopted from Amenomori et al. (2017).

and small-scale angular anisotropies.

On the other hand, a nearby passing star, blowing its wind against the headwind of the ISM, can make an efficient CR *reaccelerator* within 3–10 pc of the Sun. A synergy of the star’s bow- and wind termination shocks, *which can be supplemented by reacceleration in the stellar wind, is able to* efficiently reaccelerate the preexisting CRs. Propagating then through a turbulent magnetic flux tube pointed to the Sun, the reaccelerated CRs most naturally acquire the observed spectral features by suffering energy-dependent diffusive and convective losses from the tube.

2. Observational Challenges

2.1. Energy Spectrum

The high-precision data accumulated by several new instruments, AMS-02 (Aguilar et al. 2021a), CALET (Adriani et al. 2022b), DAMPE (An et al. 2019), ISS-CREAM, (Choi et al. 2022), challenge the CR acceleration and propagation theories. Fig. 1 shows a zoomed 10-TeV bump in an enhanced rigidity format with an extra $R^{2.7}$ factor. The data have revealed

two prominent features. The deviations from the straight power law begin with a sudden flattening at ≈ 0.2 TV. Then, the spectrum steepens back at ≈ 10 TV, also very sharply. It might then return to its low-energy slope in the 100 TV range. This spectral anomaly is a challenge since the acceleration of CRs in SNR shocks and their subsequent propagation to the heliosphere was long considered scale-invariant.

An arrow labeled R_1 in Fig. 1 shows the break rigidity. Note that the shown CALET, DAMPE, and ISS-CREAM data are adjusted to match the ISM spectrum (Boschini et al. 2020) at the minimum at $R_{min} \approx 500$ GV¹. This adjustment requires shifts in both the rigidity and normalization, which are individual for each set of data. It is not critical for our model that relies only on the shape of the CR proton spectrum. In particular, the older CALET (Adriani et al. 2019) and DAMPE data points are adjusted as described in (Malkov & Moskalenko

¹Although R_{min} appears to be a convenient visual characterization of the break position, it depends on the spectrum enhancement factor. The quantity R_1 is instead characterized by a statistically significant deviation of the data points from a power-law below the break.

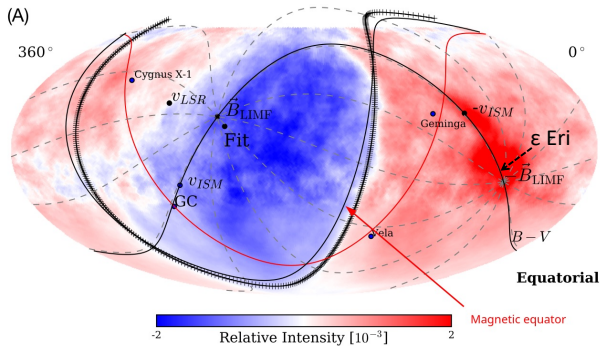


Fig. 2. CR arrival direction intensity at median primary particle energy of 10 TeV adopted from Abeyskara et al. (2019) (Fig.11a, with added arrows pointing to the magnetic equator and ϵ Eridani position.)

2022, Paper II). The adjustments used for the older CALET data are also applied to the newer CALET data set (Adriani et al. 2022b). The CREAM and ISS-CREAM data points are renormalized by a factor of 1.12 to match the CALET data (Adriani et al. 2022b).

2.2. Anisotropy

The anisotropy data shown in Fig. 1 (bottom panel) are widely interpreted as almost flat in a broad energy range between 10^{11} – 10^{15} eV, within uncertainties. This flatness is surprising, as the large-scale anisotropy is expected to grow with particle energy because they leave the Galaxy faster. Here we note, however, a striking coincidence between the energy range of the bump Fig. 1, and the anisotropy enhancement between $\approx 2 \times 10^{11}$ – 10^{14} eV, marked by a box. After that, the anisotropy briefly declines toward $\sim 10^{14}$ eV and then grows again. The enhanced anisotropy in the box area that can be primarily associated with the 10-TV rigidity bump in Fig. 2 strongly suggests the flat anisotropy being composed of two independent CR sources: the background CRs with a weak but growing anisotropy, as expected, masked by a separate component comprising the bump particles.

The overall anisotropy discussed above is at a $\sim 10^{-3}$ level, corresponding to a dipole component of CRs. There is also a small-scale anisotropy at 10^{-4} , first discovered by the Milagro observatory (Abdo et al. 2008). More accurate mapping is provided by HAWC and IceCube (Abeyskara et al. 2019). Fig. 2 shows a well-defined $\sim 20^\circ$ -wide excess likely associated with the CR prevalent arrival direction, and may very well be relevant to the 10-TeV CR bump in the rigidity spectrum shown in Fig.1. The position of the excess on the map shows that these particles are moving along the local magnetic field toward the inner galaxy. Moreover, the position of ϵ -Eridani star is at the center of the CR excess. Another striking aspect of the small-scale anisotropy, which is particularly crucial to our assertion of the proximity of its source, is a sharp increase of the CR intensity across the magnetic equator, as seen in Fig. 2. A straightforward interpretation of this increase is that particles pass the observer while moving from the outer to the inner galaxy. They have neither been scattered appreciably by the magnetic turbulence nor mirrored by it. Notably, the source

must be located somewhere not far from the observer on the outer galaxy side. We will discuss these aspects of angular anisotropy at a quantitative level in Sec. 4.

A review of recent observations of the CR anisotropy and theoretical models is given in Becker Tjus & Merten (2020). The latest data covering a relatively wide swath of the Northern and Southern hemispheres were reported by the GRAPES-3 team (Chakraborty et al. 2023). These data are largely consistent with the HAWC/IceCube small-scale counterpart of the map shown in Fig. 2. Given the close proximity of the object, which we suggest responsible for the observed anisotropy, a temporal evolution of the map compared to the earlier Milagro data is quite possible (Malkov & Moskalenko 2021, Paper I).

2.3. Secondaries

Secondary species exhibit stronger spectral hardening than the primaries (Aguilar et al. 2021a). It takes millions of years to produce the secondaries out of the primaries in CR spallation reactions. Matching the observed breaks in secondaries with additional components produced in local sources surrounded by gas clouds requires fine-tuning.

3. How Far Away the TeV-bump May Have Formed?

Whatever the reasons for the breaks, they should form not too far from us to survive smoothing by the diffusion in momentum. Using a simple relation (Skillin 1975a) between the momentum diffusivity, D_p , and the spatial diffusivity, κ , $D_p \approx p^2 V_A^2 / \kappa$, where V_A is the Alfvén velocity, one can estimate the distance to the source as follows.

A sharp break spreads in momentum by $\Delta p/p \sim \sqrt{D_p t_{\text{prop}}}/p \sim LV_A/\kappa$, where $L \sim \sqrt{\kappa t_{\text{prop}}}$ the distance to its origin and t_{prop} is the propagation time. The width Δp remains small for $L \ll \kappa/V_A$. For energies above a few GeV, $\kappa \sim 10^{28} (p/[\text{GeV}/c])^\delta \text{ cm}^2/\text{s}$, $\delta = 0.3 - 0.6$, and $V_A \simeq 30 \text{ km/s}$, we arrive at the following restriction $L_s \ll 1 \text{ kpc}$. This restriction is rigid if the first break is as sharp as the most precise AMS-02 data suggest. More importantly, since the number density of CRs at the bump is a factor of ~ 2.4 higher than the background CRs underneath it, these particles likely drive Alfvén waves by themselves. Simple estimates suggest a decrease in κ by at least an order of magnitude (Paper I). This estimate strictly limits the distance to the source to $L_s \ll 10^2 \text{ pc}$. The above estimate concerned only the propagation history of the bump. Its formation in a nearby SNR, as often suggested, must be accompanied by an even stronger spread in momentum because of an even more substantial reduction in κ around the source (Malkov et al. 2013), resulting in a delayed particle escape from its surroundings. We conclude that the bump must have formed not farther than a few tens of parsecs. However, the bump is unlikely to form inside or near the heliosphere.

As one of the angular CR enhancements discovered by Milagro (Abdo et al. 2008) was in the heliotail direction, attempts were made to explain it by the acceleration of CRs in the regions of a striped magnetic field in the heliotail. Other

peripheral magnetic perturbations around the heliosphere have also been examined. However, the 10 TeV proton gyroradius, r_g , in the 1-3 μG field is $\sim 10^3$ au, an order of magnitude larger than the heliosphere cross-section radius in its tail region, R_{hs} . CR acceleration mechanisms, based, e.g., on the reconnection in the striped magnetic field in the tail, would require $R_{\text{hs}} \gg r_g$, while an $R_{\text{hs}} \lesssim r_g$ condition is guaranteed for 10 TeV protons.

Secondary species provide another compelling argument against the nearby SNR origin of the 10-TeV bump. They exhibit a stronger spectral hardening than the primaries at the same rigidity. It indicates a rigidity-dependent modification of the spectra, possibly associated with the diffusion or diffusive reacceleration rather than the energy-per-nucleon spallation-related process, given an insufficient material grammage on the path to the observer from a nearby SNR.

The above two lines of argument imply seemingly opposite restrictions on the distance to the source of the spectral bump. On the one hand, these particles must spend a very long time in the Galaxy, thus propagating a very long distance, to process a significant ‘‘grammage’’ of the ISM gas. On the other hand, they somehow evade the momentum diffusion, which is inevitable in the turbulent ISM. The sharp spectral breaks in particle momentum distribution point to a relatively local origin of the breaks, while the underlying particles must have been accelerated in distant objects, most likely an ensemble of SNRs, to process sufficient grammage. The most natural way to reconcile this contradiction is to assume that the bump comprises *locally reaccelerated* background CRs.

Alternatively, matching the Galaxy-wide spectra with the local-source-produced component requires fine-tuning the local source abundances, its surrounding gas grammage, and the rigidity dependence of the diffusion coefficient in the whole Galaxy (e.g., Qiao et al. 2023). Apart from the fine-tuning and multi-source invocation, it is not clear whether the respective models fit the high-fidelity data shown, e.g., in Fig.1 (top panel). These models typically span 2-4 orders of magnitude in the CR flux (multiplied by $R^{2.7}$), as opposed to the factor $\simeq 1.5$ shown in the figure. As can be gleaned from Fig.2, the presumed magnetic connectivity of the suggested local sources, such as Geminga, (e.g., Zhao et al. 2022), is questionable for at least two reasons. First, its position on the CR map is not well aligned with either the local field direction or the CR hot spot, which is in striking contrast with the ε Eridani. Second, the field direction at the sun is almost certainly irrelevant to that at any source outside of the Local Bubble, such as Geminga SNR. This lack of magnetic connectivity owes to the diamagnetic flux expulsion during the Local Bubble formation by a series of SN explosions some millions of years ago. We will discuss other models of the 10-TV bump origin outside of the Local Bubble in Sec.5.

4. Plausibility of the Local Origin of 10-TeV Bump

4.1. Rigidity Spectrum

Suppose a stellar bow shock is moving through the ISM, Fig. 3. At any instant, it populates a particular magnetic flux

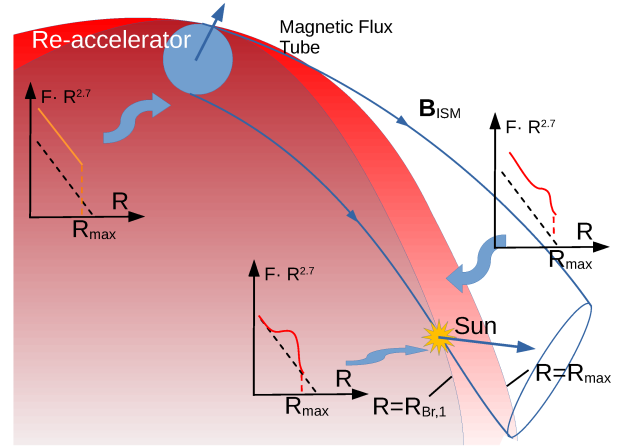


Fig. 3. Schematics of a moving CR reaccelerator (e.g., a stellar bow shock–wind termination shock) and reaccelerated CRs that diffuse predominantly along the field lines, thus forming a wake behind this object. Three types of reaccelerated CR spectra are shown at different positions in the wake. Dashed black lines show the CR background spectrum in each of the three insets schematically showing the observed total spectra (solid lines), depending on the observer’s position in the stellar wake (see text). The edge of the broader shaded area marks the boundary which the reaccelerated particles with $R = R_{\text{max}}$ can reach, while those with $R < R_{\text{max}}$ can not. Outside of the inner shaded area, particles with $R < R_1$ cannot be observed. The Sun is located at this edge.

tube with CRs reaccelerated up to R_{max} . This quantity is limited by the requirement that Larmor radii of these particles $r_g = cR_{\text{max}}/B$ do not exceed the bow-shock size. The latter may extend up to $\sim 10^4$ au (Wood et al. 2002). An enhanced magnetic field blown out of the stellar cavity and compressed around the apex of the bow shock may significantly ease this constraint. Particles, reaccelerated at the bowshock and the stellar wind termination shock then propagate primarily along the tube to a distance increasing with their rigidity. While moving further through the ISM, the star leaves a turbulent wake of flux tubes filled with reaccelerated CRs. It continues to broaden along and across the field with the strongly different diffusivities $\kappa_{\parallel} \gg \kappa_{\perp}$. These quantities are related to the ISM frame, assuming that there is no bulk fluid motion in the wake. At any given distance behind the star, the breadth of the wake depends on the particle rigidity. Therefore, depending on the position of the observers in the wake, they will see the reaccelerated particles in the range $R_1 < R < R_{\text{max}}$. Here, R_{max} is the maximum rigidity attainable by the reacceleration. At the sun position, particles with $R < R_1$ (the first break, Fig.1) have not reached the observation point yet, as they diffuse slower. As mentioned above, the wake also has its thickness in the direction across the plane fixed by the star velocity and magnetic field vectors. Here, we ignore it by assuming that the sun is well inside the wake in this direction.

Assume further the Sun is in the wake where only particles with rigidities $R \geq R_1$ can reach (the first break, see Fig.

3). We, therefore, see the spectrum flattening at $R > R_1$. The Sun's position in the wake and the energy upshift due to the reacceleration shape the bump appearance (shown in the bottom spectrum in the figure). These model parameters fix its magnitude (factor ≈ 2.4 above the background) and its rigidity (~ 10 TV), while the details of reacceleration are less critical. We can get a glimpse into the spectrum variations at higher rigidities in the flux tube using Eq. (1) below. In particular, the second break at $R = R_2$ (close to the maximum at $\approx 10^4$ GV in Fig. 1) forms where the diffusion of reaccelerated CRs along the tube exceeds their convection with the ISM flow out of the tube. The spectrum slope becomes close to that it has at and behind the shock surface. At yet higher rigidities it approaches that of the CR background, especially when the CR losses out of the tube dominate.

The acceleration depends on the local angle between the shock normal and the magnetic field: quasi-perpendicular shock ($\vartheta_{nB} \approx \pi/2$), vs. quasiparallel shock ($\vartheta_{nB} \ll 1$). A dull cone-shaped stellar bow shock makes a wide range of angles to the local field, $\vartheta_{nB} \leq \pi/2$, with a possible exception for $\vartheta_{nB} \ll 1$. Even a weak quasi-perpendicular shock ($\vartheta_{nB} \approx \pi/2$) of a size exceeding the particle Larmor orbit can provide the necessary energy upshift, operating in a shock-drift acceleration (SDA) regime. All it takes is that the shock overruns a significant portion of the particle's Larmor orbit before the particle escapes the shock front along the field line. A single complete orbit crossing takes $r_g/U_{\text{shock}} \approx 30$ yrs for $r_g \sim 3 \cdot 10^{15}$ cm (a 10 TV proton in a 10 μ G field) and $U_{\text{shock}} \approx 30$ km/sec. Note that direct Voyager 1, 2 measurements give 7–8 μ G just outside the heliosphere (Burlaga et al. 2019). As mentioned earlier, stars with winds more powerful than solar, such as the ϵ Eridani star discussed in Paper I, likely have a stronger field outside the astrosphere due to the Axford-Cranfill effect. It constitutes a magnetic pillow made of the stellar magnetic field blown out by the wind.

The reacceleration requirements are relatively mild. The bump height with respect to the underlying background spectrum at $R \approx 10$ TV is a factor of 2.4. However, because the background spectrum is relatively steep ($\gamma_b \approx 2.85$), it suffices to reaccelerate the background particles with the initial rigidity $R \approx 10/1.4 \approx 7.1$ TV to $R \approx 10$ TV, which will elevate the level at 10 TeV by the required factor of 2.4. A particle energy gain after its Larmor circle orbit is crossed by a shock can be calculated from the condition of adiabatic compression: $p_{\perp}^2/B = \text{const}$, where p_{\perp} is the perpendicular to the magnetic field component of particle momentum. Therefore, even a factor of 2-3 shock (magnetic field B) compression would suffice to make the bump visible. The momentum gain should further increase due to the Axford-Cranfill effect. It should be noted that the wake itself is formed primarily by the shocked stellar wind blown by a star with a mass loss rate at least 30 times the solar one. The flow past the termination shock is likely to be highly turbulent, thus offering additional mechanisms of reacceleration. They are worth a separate study.

Consider now an oblique portion of the bow shock to demonstrate a straightforward possibility of CR reacceleration. We will add to the standard DSA scheme (Blandford & Ostriker

1978) losses from the flux tube, which are essential at higher rigidities, $R > R_L$. The result of reacceleration can then be cast as (Paper I, Paper II):

$$f_{\text{CR}}(R) = A_b R^{-\gamma_b} \left\{ 1 + \frac{\gamma_b + 2}{q_s - \gamma_b} \exp \left[- \left(\frac{R_0}{R} \right)^a - \sqrt{\frac{R}{R_L}} \right] \right\}. \quad (1)$$

Here γ_b (e.g., ≈ 2.85 for protons) and A_b are the known background CR index and normalization factor, respectively, q_s is the shock spectral index $q_s = (r+2)/(r-1)$, where r is the shock unknown compression, $R_0 \propto (L_s W / \sqrt{l_s})^{1/a}$ is the characteristic bump rigidity that depends on the unknown distance to the shock, L_s , its size, l_s , and the level of turbulence in the flux tube, W , and, especially, its index a (see below). The **three fundamental unknown bump-specific CR fitting parameters** q_s , R_0 , and R_L (Table 1), can be obtained from fitting Eq. (1) to the proton spectrum (Fig. 1), the best measured among CR species. Therefore, our model needs only three parameters, which is two times less than the required minimal number of simple geometric parameters defining the bump shape, which is equal to **six** (Paper I). Moreover, as the spectrum is given in the element-invariant rigidity form, the same fitting parameters derived from the proton spectrum can be used to predict the spectra of other elements, such as He, C, O, etc., and the secondaries with **no free parameters** (Paper II). Each CR species has its fixed known input parameters A_b and γ_b derived from their local ISM spectra below the bump, different from those of CR protons, see Sect. 4.2.

However, the most critical parameter for the fit is the turbulence-related index a in the flux tube: $W_k \propto k^{a-2}$, where W_k is the wave spectral density. For calculations shown in Fig. 1, we have determined it from dimensional reasoning to be $a = 1/2$, which corresponds to the Iroshnikov-Kraichnan (IK) turbulence model, $k^{-3/2}$. Still, as we have used only three fitting parameters in Eq. (1) out of the six that are required for a full bump characterization, we can verify our calculation of a by minimizing the data mismatch. The mismatch has a very sharp minimum near $a = 1/2$ (Paper I).

Moreover, the fit presented in Fig. 1 for $a = 1/2$ (Paper I) rules out other popular turbulence models, entertained in CR acceleration and propagation studies, such as $1/k$ (Bohm model) and $k^{-5/3}$ (Kolmogorov model). In particular, the Kolmogorov and Goldreich-Shridhar spectra do not fit the new high-fidelity data, shown in Fig. 1. These spectra will likely dominate the ISM turbulence outside the flux tube. The fit does not call them into question since the IK spectrum is derived for a specific CR driver in the flux tube. Even more significant deviation from the data gives the Bohm turbulence regime, which, in turn, is expected closer to the shock that reaccelerates CRs but does not contribute to their propagation over the entire tube length. Our results thus point to the CR-filled flux tube (or its wake) from a set of choices for explaining the 10-TeV bump phenomenon. It most likely connects the Sun with a CR-reaccelerating shock 3-10 pc away.

4.2. Heavier CR species

According to Eq. (1), the CR species are differentiated solely by their spectral index γ_b below the first break R_1 , which is fixed

Table 1. Model parameters and fit results for the proton spectrum.

Parameter (St. err. %)	$R_0(\text{GV})$	$R_L(\text{GV})$	q_s
Realistic Model (RM)	5878 (3.5%)	2.24×10^5 (28%)	4.20
Loss-Free Model (LF)	4794 (3.2%)	∞	4.73

Table 2. Input parameters for CR species derived from their LIS (Boschini et al. 2020, 2021) at ≈ 100 GV.

Parameters	H	He	B	C	O	Fe
A_b ($\text{m}^{-2} \text{s}^{-1} \text{sr}^{-1} \text{GV}^{-1}$)	2.32×10^4	3631	70.2	111	108	11.6
γ_b	2.85	2.77	3.09	2.75	2.73	2.66

by the data. We derive γ_b from a fit to the LIS by Boschini et al. (2020, 2021) at $R \approx 100$ GV (Table 2). On one hand, this is significantly below the break rigidity R_1 and is thus representative for the background spectrum. On the other hand, the solar modulation at such rigidity is fairly weak. Meanwhile, a straight fit to the data would produce very similar values.

We illustrate this in Fig. 4 that shows proton, He, B, C, O, and Fe spectra. The proton spectrum is the same as in Fig. 1. CALET B, C, O, Fe data are renormalized up by a factor of 1.3 to match AMS-02 data, while CALET He data (Adriani et al. 2023) and data by other instruments are not adjusted. Given almost the same spectral indices for He, C, O below the first break R_1 , their spectral shapes are identical. We also show the

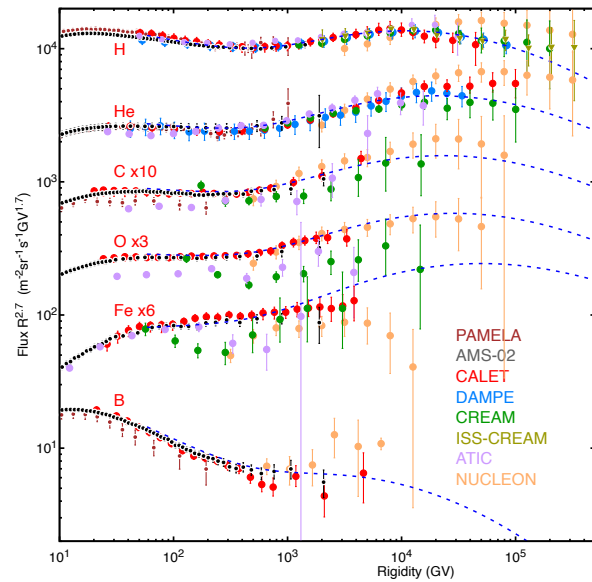


Fig. 4. Spectra of CR species: protons, He, B, C, O, Fe. The compilation of data includes AMS-02 (Aguilar et al. 2021a,b), ATIC (Panov et al. 2009), CALET (Adriani et al. 2019, 2020, 2021, 2022b,a, 2023), CREAM (Ahn et al. 2009, Yoon et al. 2017), DAMPE (An et al. 2019, Alemanno et al. 2021), ISS-CREAM (Choi et al. 2022), NUCLEON (Karmanov et al. 2020b,a, Grebenyuk et al. 2019), and PAMELA (Adriani et al. 2011) instruments. The proton spectrum is plotted as in Fig. 1. CALET B, C, O, Fe data are renormalized up by a factor of 1.3 to match the AMS-02 data, while the CALET He data are not adjusted. The blue dashed lines show the local ISM spectra Eq. (1) in the realistic model with losses (Paper II), Tables 1 and 2.

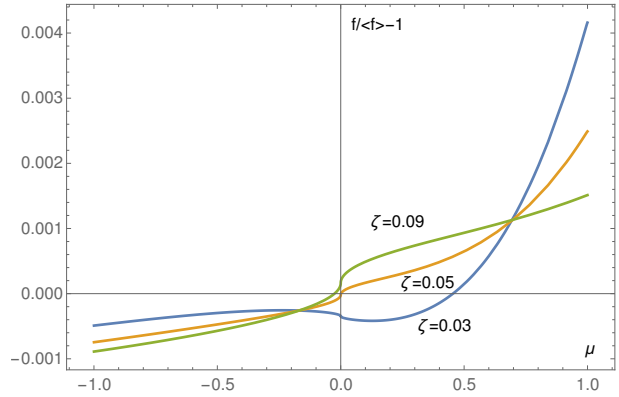


Fig. 5. Three solutions as a function of μ shown as a relative anisotropy, $(f - \langle f \rangle) / \langle f \rangle$. The isotropic part $\langle f \rangle \approx 0.50$ for all three values of ζ , and decreases with ζ insignificantly, since $v_{\perp} = 10^{-6}$ and $\lambda_0 \approx 0.00447$, $\lambda_1 \approx 45.0$, $\lambda_2 \approx 132$. The source anisotropy $Q_1(\chi) = 1 + 0.01|\chi|^3$, introduced by writing the source Q in eq.(2) as $Q = v_{IK} Q_0(p) Q_1(\mu)$. Eigenmodes decay with distance as $f_n \propto \exp(-\lambda_n |\zeta|)$.

spectra of B and Fe, which have different spectral indices below the first break R_1 . Spectra of all species show good agreement with available data. Good quality data for B and Fe around the second break R_2 are desired, but not available yet due to the low flux and thus limited statistics. When available in the future, they could be used to discriminate between models.

4.3. Anisotropy

If the shock is located at a few particle's mean free paths from the observer, a sharp increase in the CR intensity across the magnetic equator is expected and was indeed observed in Abeyskara et al. (2019), Fig. 2.

We use the Fokker-Planck equation for the CR propagation along the field (Paper I):

$$c\mu \frac{\partial f}{\partial \zeta} + v'_{\perp} f - \frac{\partial}{\partial \mu} \left((1 - \mu^2) \mathcal{D}(p, \mu) \frac{\partial f}{\partial \mu} \right) = Q(p, \mu) \delta(\zeta). \quad (2)$$

Here μ is the pitch angle cosine of a particle with momentum p . The spatial coordinate ζ is directed along the field, and the source is at the origin. The other two coordinates are removed by averaging the distribution function across the flux tube. The particle flux through its boundary enters as $v'_{\perp} f$ on the l.h.s. The CR scattering frequency \mathcal{D} is related to there

Alfvén wave fluctuations E_k^A , by an IK spectrum. The solution is found by decomposing it in a series of eigenfunctions of the operator on its l.h.s. Starting from some distance from the source, it is dominated by the lowest eigenvalue $\lambda_0 \approx 2\sqrt{5}v_\perp$ and can be approximated near magnetic equator as $f_0 \approx \sqrt{5/\lambda_0} \left[1 + (\lambda_0/4) |\mu|^{1/2} \text{sgn}\mu \right]$, thus showing a sharp increase over the magnetic equator ($\mu = 0$), consistent with the data presented in Fig. 2. Here, we have introduced the loss rate $v_\perp = |\mu|^{1/2} v'_\perp / v_{\text{IK}}$, assuming it μ - independent. The Iroshnikov-Kraichnan scattering rate is, in turn, related to the pitch-angle scattering rate \mathcal{D} in eq.(2) as follows: $\mathcal{D} = 4v_{\text{IK}} |\mu|^{1/2}$. Further details of the analysis of this equation can be found in the above reference. Note that the Kolmogorov turbulence would produce a steeper rise of CR intensity across the magnetic equator, $\propto |\mu|^{1/3} \text{sgn}\mu$, which might become discernible from the IK turbulence if the HAWC-IceCube statistics improve. At the same time, an isotropic pitch angle scattering that results in a Bohm diffusion regime would produce no such effect at all, as the scattering frequency is analytic ($\mathcal{D}(\mu) \approx \text{const}$) at $\mu = 0$. Besides, this can be seen from an exact solution of the underlying Fokker-Planck equation (Malkov 2017). We also note here that the three turbulence models discussed above are abundantly present in the solar wind (Chen et al. 2020).

The small-scale anisotropy ($f_{n \geq 1}$) can also be observed at the dimensionless distance to the source $|\zeta| \lesssim 1/\lambda_1$, along with the sharp increase across the magnetic equator discussed in the preceding paragraph. To illustrate the variation of small- and large-scale anisotropy with the distance, we show in Fig. 5 the angular distributions of CRs at three different dimensionless distances ζ (given in units of c/v_{IK}). At a short distance ($\zeta = 0.03$), there is a strong increase in the field-aligned particles ($\mu \approx 1$), but the curve is inconsistent with the observed map (Fig.2) at $\mu = 0$. For large distances ($\zeta = 0.09$), the behavior at $\mu = 0$ is correct, but there is not significant enhancement at $\mu = 1$, observed in B_{LIMF} direction. Only at $\zeta = 0.05$, both effects are consistent with the observations. We thus see that when ζ decreases by a factor of 3 (from 0.09 to 0.03), the CRs dipolar distribution shrinks to a sharp one toward the source. It shows a progressively stronger CR field alignment. Along with a jump across the magnetic equator at $\mu = 0$, contained in f_0 , an enhancement at $\mu \approx 1$, associated with f_1 , is observed at the distances $0.05 < \zeta < 0.1$. This angular pattern can be found on the map of CR arrival directions in Fig. 2. Its interpretation based on the ε -Eridani proximity naturally explains the puzzle of CRs predominantly arriving from the Galactic ANTI-center direction. At the same time, γ -ray observations of the diffuse emission by *Fermi*-LAT testify to a higher concentration of CRs in the inner Galaxy (Ackermann et al. 2012, Zhang et al. 2023), see also Gabici (2023). By contrast, even an advanced propagation model (Chernyshov et al. 2023) based on distributed CR sources is unlikely to reproduce the sharp, especially Galactic anti-center prevalent CR anisotropy. We will discuss the alternative models in Sec.5.

4.4. γ -rays from ε Eridani

Interestingly, there is an indication of the γ -ray emission in the direction of the proper motion of ε Eridani (RA: -974.758 mas/yr, Dec: 20.876 mas/yr, Gaia Collaboration 2020) at a distance of $\lesssim 0.5^\circ$, which corresponds to the size of the astrosphere and the location of the bow shock. Fig. 3 in Riley et al. (2019) shows the position of ε Eridani with the white circle in the middle of the $10^\circ \times 10^\circ$ region of interest. An excess emission to the right of the star (the direction of the proper motion) is marked with a green circle *partially* overlapping with the white circle, but the spectrum of the excess emission is not provided. The soft spectrum of the emission from *the star* may suggest background contamination rather than reflecting emission from the star itself. Riley et al. (2019) speculate about the emission from interactions of cosmic rays with the debris disk around the star or the stellar activity. Unfortunately, the angular resolution of *Fermi*-LAT in the analyzed energy range 100 MeV – 3.16 GeV is *rather* poor and does not allow us to reconstruct further details.

5. Alternative Explanations of the 10-TeV CR Bump

The now firmly established 10-TeV bump phenomenon has been emerging for more than a decade following improvements in observations. The first reports on spectral hardening in the p-He spectra at a few 100 GV date back to the mid-2000s (for an abbreviated list of references see, e.g., Paper I). The full appreciation of its realism and significance was gained only a few years ago, after the accuracy of the spectral data was significantly improved. This allowed the AMS-02 (Aguilar et al. 2015) and CALET (Adriani et al. 2019) teams to quantify the spectral hardening by measuring the sharpness of the transition in the proton spectrum, $s = 0.024 \pm_{0.021}^{0.034}$ and 0.089 ± 0.133 , correspondingly, using the fitting function:

$$F_{\text{CR}} \propto R^{-\gamma} \left[1 + (R/R_{\text{br}})^{\Delta\gamma/s} \right]^s. \quad (3)$$

Here γ is the spectral index below the break, and $\Delta\gamma$ is the value of the spectral break. The sharpness of the break was also confirmed with larger statistics, $s = 0.09 \pm_{0.03}^{0.04}$ (AMS-02, Aguilar et al. 2021a). Further critical insight has been gained from more precise measurements of other elements, especially the secondary ones, as well as from the detailed angular distribution of the protons around 10 TeV.

At first, the emerging discovery was perceived as an isolated spectral hardening and triggered suggestions of two unrelated mechanisms for its explanation. The first mechanism was a straightforward combination of two or more independent CR sources, such as nearby SNRs, including the CR background power-law spectrum. With significant error bars attached to the data sets, these models were consistent with the shape of the primary CR spectra. However, persuasive arguments (Vladimirov et al. 2012) have promptly pointed to a likely inconsistency of these models with even more substantial hardening observed in the spectra of secondary CR species. If the primary nuclei produced them after being accelerated in the nearby sources, an unrealistically large amount of target

material for the spallation reactions between the source and the observer would be necessary.

The second mechanism seemingly circumvents the problem with secondaries by invoking a presumed break in the turbulence spectrum that controls particle transport (Vladimirov et al. 2012). The recent review of this mechanism and the list of references can be found in Blasi et al. (2022), whereas interesting new approaches were published afterward (Chernyshov et al. 2022, 2023). According to the models built on this premise, the break in the turbulence spectrum at the wave number k_{br} directly translates into the break in the momentum spectrum of propagating particles at $p_{br} = eB/ck_{br}$, because of this cyclotron resonance condition. Breaks in the ISM turbulence spectra are possible, and such breaks are even observed in the solar wind *in situ* (Chen et al. 2020). However, there are three aspects of particle propagation not included in these models, whereby the turbulence break *will not be mirrored* in the observed *sharp break* in the particle momentum spectrum. We describe them below.

5.1. The Spectral Break is too Sharp to form Remotely

Were the observed CRs propagated a significant distance to us, a sharp spectral break would be smeared out over the momentum range $\Delta p \gtrsim p_{br}$, as we have argued at the beginning of Sec.3. The observed break requires the opposite condition $\Delta p \ll p_{br}$ that indicates a closeby source responsible for the break. In fact, the parameter $\Delta p/p_{br}$, whose numerical equivalent was denoted by s , Eq. (3), was directly obtained from the observations (also shown in Fig. 1 above) being $s \approx 0.1$. It should be noted here that the expression in eq.(3) is *ad hoc*, unlike Eq. (1). The latter results from solving a particle reacceleration problem and is used for the fit shown in Fig. 1. Nevertheless, the above formula for F_{CR} in Eq. (3) provides a helpful tool for ruling out a broad range of models, including those discussed at the beginning of this section.

We illustrate this point in Fig. 6. It shows fits to the AMS-02 CR proton data (Aguilar et al. 2021a). The original fit (45 GV–1.8 TV, Aguilar et al. 2021a) with functional dependence given in Eq. (3) is shown by the black solid line, where the numerical values of parameters are slightly adjusted. Such a fit requires a fairly small value of $s \approx 0.09$. The latter means that the two power laws, at low and high energies (solid green lines), should have a sharp cutoff near the break rigidity. Otherwise, a simple sum of the two power-laws, the combined spectrum ($s = 1$), is too broad to fit the data. The sum of these power-laws is shown by the blue solid and dotted lines for different normalizations.

5.2. Artificial Resonance Sharpening Produces the Break Artifact

A sharp break in the turbulence spectrum produces only a smooth variation of the power-law index in the particle momentum spectrum during their propagation through the turbulent ISM. This relation between the two breaks, which follows from the character of particle interactions with resonant magnetic perturbations, is often overlooked in the literature.

Consider a circularly polarized Alfvén wave with the wave number k propagating along the magnetic field. This setting is

most favorable and straightforward for connecting the breaks in wave and particle spectra directly. In the wave’s rest frame, a particle spiraling around the unperturbed field with an average velocity v_{\parallel} perceives an oscillatory force from the wave of the frequency $kv_{\parallel} \equiv kv\mu$, where μ is the cosine of the particle’s pitch angle and $v \approx c$. An irreversible pitch angle variation occurs when the particle passes a cyclotron resonance that, for ultrarelativistic particles, can be written as $p = eB/ck\mu$. It involves one wave parameter, k , and two parameters for the particles, p and μ .

However, typical models that associate the wave spectral breaks with those of the particles use a simplified resonance condition, $p \approx eB/ck$, involving one-to-one wave-particle resonant association. This simplification was introduced by Skilling (1975b) out of “algebraic convenience” and called “resonance sharpening.” While broadly used and helpful in studying smooth particle and wave spectra, it is inadequate for treatments of broken ones, especially the sharply broken spectra discussed above. Indeed, it effectively collapses a nearly isotropic particle distribution in μ to a delta-like distribution at some $\mu = \mu_0 \simeq 1$. To demonstrate the inadequacy of this approximation for sharply broken wave spectra, consider two particles with different momenta p_1 and $p_2 > p_1$. According to the “sharpened” resonance conditions, each of them interacts with a unique wave with $k = k_1$ and $k = k_2 < k_1$. Therefore, if there is a break in the wave spectrum somewhere between k_2 and k_1 , a corresponding break is expected to form in the particle spectrum between p_2 and p_1 .

If the exact resonance condition, $p = eB/ck\mu$, is applied instead, two particles with momentum p_1 but with different μ may interact with both k_1 and k_2 waves, which is also true for the particles with momentum p_2 . Therefore a break in the wave spectrum will not profoundly affect the particle spectrum. To put it formally, consider the wave-particle interaction term in a quasilinear approximation, which in a particle kinetic equation appears in the form $\int dk \delta(p\mu - eB/ck) W_k(\dots)$. Here W_k is the wave energy density. We denoted components of the matrix element of the wave-particle interaction unessential for this discussion by (\dots) . Eventually, pitch-angle scattering translates into particle diffusion. The argument behind the formation of the spectral break in the particle spectrum is that the break should form in the particle diffusion coefficient in the first place. However, this does not happen, which can be readily seen from the following quasilinear result for the particle diffusion coefficient (Kulsrud & Pearce 1969):

$$\kappa_{\parallel}(p) = \frac{cB^2 p^2}{m^2 \omega_c^2} \int \frac{|\mu| (1 - \mu^2) d\mu}{W_{k=eB/cp\mu}}. \quad (4)$$

Representing the integral as

$$\int \frac{p\mu^2 (1 - \mu^2) d\mu dk}{W_k} \delta\left(kp\mu - \frac{eB}{c}\right) = \int \frac{\mu_k^2 (1 - \mu_k^2) dk}{kW_k},$$

where $\mu_k \equiv eB/cpk$, reveals any kink (discontinuity in a derivative) in the turbulence spectrum W_k being smoothed out after the integration over k . The discontinuity of $\partial W_k / \partial k$ at $k = k_{br}$ will then translate only in the discontinuity of

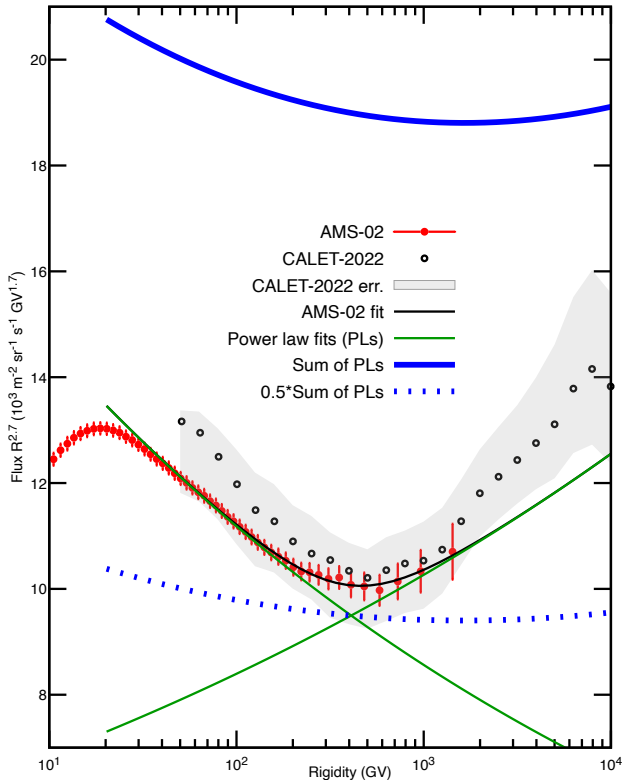


Fig. 6. Illustration of fits to the AMS-02 CR proton data (Aguilar et al. 2021a). The original fit (Aguilar et al. 2021a) with functional dependence given in Eq. (3) is shown with the black solid line, where the numerical values of parameters are slightly adjusted. For clarity, only CALET data at high energies are shown. The asymptotic power laws at low ($\propto R^{-\gamma}$, $\gamma \approx -2.8$) and high ($\propto R^{-\gamma+\Delta\gamma}$, $\Delta\gamma \approx 0.2$) rigidities derived from Eq. (3) are shown by the green lines. The solid blue line represents their sum, while the dotted one shows a half of that, for comparison. It is clear that no curve in between would match the composite AMS-02/CALET data.

$\partial^2 \kappa_{\parallel} / \partial p^2$ at $p = p_{\text{br}}$, thus rendering no break in $\kappa_{\parallel}(p)$ and a correspondingly smooth particle spectrum. Asymptotically, at $p \gg p_{\text{br}}$, the particle spectral slope will accommodate to the different slope of W_k at $k < k_{\text{br}}$. However, the transition will occur over a broad region $\Delta p / p_{\text{br}} > 1$, contrary to the observations. On a positive note, this gradual spectral flattening is consistent with the CR observations in the knee area at PeV energies, thus having some potential for describing the behavior of the CR spectrum over the momentum scales 1 TeV – 1 PeV, but clearly inconsistent with sharp spectral variations in the TeV range.

5.3. Effect of Nonlinear Landau Damping on Sharp Spectra

Another common element of the models that attempt to translate a break in the turbulence spectrum to that in the particle momentum spectrum is the so-called nonlinear Landau damping. From the wave perspective, this is the process of wave scattering on the plasma thermal particles: $\omega, k \rightarrow \omega', k'$ and hence, another name for the process is “induced scattering” (Sagdeev & Galeev 1969, Lee & Völk 1973). From the particle perspective, it describes the thermal particle scattering on a beat wave with the frequency $\omega \pm \omega'$ and wave vector

$k \pm k'$. This process is essentially a higher-order approximation in the expansion of the wave-particle interaction in the wave amplitude, following the standard quasilinear treatment and resulting in $\sim W_k^2$ terms in the wave kinetic equation. Given the linear dispersion of long Alfvén waves, $\omega = k_z V_A$, it is clear that Alfvén waves from a broad k -range generate beat waves with phase velocities resonant with the thermal particles. It follows then that the concept of “resonance sharpening” is even less suitable for the induced scattering than for the lower order approximation described above. In most of the models addressing spectral hardening, this process is included in an oversimplified, integrated form that does not adequately describe the particle resonance with beat waves (cf. Chernyshov et al. 2022 and Lee & Völk 1973).

A more general smoothing effect on any possible break in the CR momentum spectrum created in a significant volume of galactic disc and adjacent halo is the following. Assume that despite the above arguments, the CR break is created at some $p = p_{\text{br}}$. As it must be produced by a change in the particle transport regime (diffusion, convection, field-line streaming, and escape), the value of p_{br} must depend on the local parameters which vary considerably across the galaxy volume. So the momentum derivative of the broken power law will be $\partial F_{\text{CR}} / \partial p \propto F'(p, r) + \alpha(p, r) \Theta[p - p_{\text{br}}(r)]$, where Θ is the Heaviside unit function and F' and α are continuous functions. Since we are observing particles that come to us from at least a kpc distance, we must average this result over the respective volume. The averaging will smear out the jump in the Heaviside function and, therefore, the break in F_{CR} .

To conclude this section, we reiterate that, in addition to the above arguments, the second-order Fermi reacceleration must smear out *any sharp break* formed at distances longer than a few hundred parsecs. The neutral gas damping of the ISM turbulence is unlikely to suppress the reacceleration since the Local Bubble plasma (~ 100 pc) is highly ionized. Only the local cloud network may produce some damping effect, but it constitutes only an insignificant (~ 10 pc) fraction of the Local Bubble on the CR propagation path.

6. Conclusions and Discussion

We have analyzed the high-fidelity data on the 10-TeV puzzling bump in the Galactic rigidity spectrum. It likely originates from 3-10 pc of the Sun. A system of bow-plus-termination shocks associated with a star, such as ϵ Eridani, possibly supplemented with its notably powerful stellar wind, is capable of significant CR reacceleration. Being magnetically connected with the Sun, the ϵ Eridani system likely accounts for all observed bump features well within the data uncertainties with only three free parameters derived from a fit to the proton spectrum. A significant number of such features discussed make a coincidental agreement *rather* unlikely. Any combination of primary CR sources, such as SNRs, and variations in the CR propagation cannot account for the fine angular and energy spectral structures. The resultant CR spectrum would be smoother than observed since these sources are at least a few 100 pc away.

Observations of CRs in an intermediate energy range from 0.1–100 TeV are becoming increasingly instrumental in testing models for CR acceleration and propagation, as this is their preferred territory, void of difficulties associated with particles entering the acceleration (injection of suprathermal particles) and escape after achieving the highest energy possible for the presumed accelerators, such as SNR shocks. Even more critical is the multifaceted character of the newest observations, cutting across the rigidity, angular, and multispecies aspects of the CR spectra in this range, thus helping us zero in on the most tenable models. Regarding the model discussed in this paper, we adhered to the following requirements:

1. Fitting the bump rigidity spectrum, shown in the log-linear² format with the $R^{2.7}$ factor within minimal for a given rigidity error bars, complementarily selected from the high-fidelity instruments. A formal description of the bump requires six parameters (two rigidity values, two index variations, and two sharpness parameters for each break in the spectrum). The number of model parameters should thus be less than 6. Our model uses just 3 parameters that encapsulate the distance/size of the accelerator (shock), its strength, and particle losses from the flux tube during their propagation to the observer.
2. Explaining both the sharp anisotropy in the bump CR arrival directions across the local magnetic equator and its dipolar component. They both point to the source located in the hemisphere opposite to the Galactic center.
3. Explaining why the secondary CRs develop a somewhat stronger first break than the primary CRs do. Note that the second break has not been seen in the secondaries yet due to their soft spectra and thus insufficient statistics at multi-TV rigidities, but this may change soon.
4. Demonstration of intervening turbulence not smoothing out the bump during the CR propagation from its source to the observer. Demonstration of the turbulence index consistency with the bump shape.
5. Demonstration of magnetic connectivity with the source of CRs constituting the bump; alternatively, the bump has to be devised to be generated in a large volume of the Milky Way containing the heliosphere. This scenario would encounter insurmountable problems with the model requirements (1-4).

6.1. Challenge to the Model

A concern may be raised about the ε Eridani bow shock–wind termination shock system, which may be perceived as being too small ($\sim 10^4$ au $\approx 1.5 \times 10^{17}$ cm) for modifying the CR spectrum around the 10-TeV energy to the observed bump amplitude (proton gyroradius $\approx 3 \times 10^{15}$ cm in 10 μ G field). In addition to the arguments made in Sec. 4 about a relatively weak acceleration required, this problem can further

be ameliorated by recent findings about the current Sun position relative to the local clouds and the direction to ε Eridani. Namely, once the CRs are reaccelerated at the ε Eridani, they must pass to the Sun between the G-Cloud (which is in the Galactic center direction as seen from the solar system) and the Local Interstellar Cloud (LIC). Moreover, the Sun no longer resides in the LIC, as previously believed, but is already in the LIC-G-cloud interaction medium (Swaczyna et al. 2022). If so, the field extraneous to both clouds is then compressed by their motion towards each other with a relative velocity ≈ 7.2 km/s. The field was known to be tangent to both cloud surfaces (Lallement et al. 2005), thus most likely being, indeed, compressed by them. The compressed intercloud field must create a magnetic focusing effect on the CR passing the Sun, currently crossing the G-LIC interface. The magnetic focusing should increase the CR flux through the flux tube, thus facilitating the fit. Quantifying this increase merits a separate study.

Acknowledgments

We thank two anonymous referees for their helpful comments. Work of MM, PD, and MC is supported by NSF grant AST-2109103, and, in part, by NASA ATP 80NSSC24K0774. IM acknowledges partial support from NASA grants 80NSSC23K0169 and 80NSSC22K0718.

References

- Abdo, A. A., Allen, B., Aune, T. et al. (2008). Discovery of localized regions of excess 10-TeV cosmic rays. *Phys. Rev. Lett.*, *101*(22), 221101–+. doi:10.1103/PhysRevLett.101.221101. arXiv:0801.3827.
- Abeysekara, A., Alfaro, R., Alvarez, C. et al. (2019). All-sky measurement of the anisotropy of cosmic rays at 10 TeV and mapping of the local interstellar magnetic field. *Astrophys. J.*, *871*(1), 96.
- Ackermann, M., Ajello, M., Atwood, W. B. et al. (2012). Fermi-LAT observations of the diffuse γ -ray emission: Implications for cosmic rays and the interstellar medium. *Astrophys. J.*, *750*(1), 3. doi:10.1088/0004-637X/750/1/3. arXiv:1202.4039.
- Adriani, O., Akaïke, Y., Asano, K. et al. (2019). Direct measurement of the cosmic-ray proton spectrum from 50 GeV to 10 TeV with the Calorimetric Electron Telescope on the International Space Station. *Phys. Rev. Lett.*, *122*(18), 181102. doi:10.1103/PhysRevLett.122.181102. arXiv:1905.04229.
- Adriani, O., Akaïke, Y., Asano, K. et al. (2020). Direct measurement of the cosmic-ray carbon and oxygen spectra from 10 GeV/n to 2.2 TeV/n with the Calorimetric Electron Telescope on the International Space Station. *Phys. Rev. Lett.*, *125*(25), 251102. doi:10.1103/PhysRevLett.125.251102. arXiv:2012.10319.
- Adriani, O., Akaïke, Y., Asano, K. et al. (2022a). Cosmic-ray Boron flux measured from 8.4 GeV/n to 3.8 TeV/n with the Calorimetric Electron Telescope on the International Space Station. *Phys. Rev. Lett.*, *129*(25), 251103. doi:10.1103/PhysRevLett.129.251103. arXiv:2212.07873.
- Adriani, O., Akaïke, Y., Asano, K. et al. (2023). Direct measurement of the cosmic-ray helium spectrum from 40 GeV to 250 TeV with the Calorimetric Electron Telescope on the International Space Station. *Phys. Rev. Lett.*, *130*(17), 171002. doi:10.1103/PhysRevLett.130.171002. arXiv:2304.14699.
- Adriani, O., Akaïke, Y., Asano, K. et al. (2022b). Observation of spectral structures in the flux of cosmic-ray protons from 50 GeV to 60 TeV with the Calorimetric Electron Telescope on the International Space Station. *Phys. Rev. Lett.*, *129*, 101102. URL: <https://link.aps.org/doi/10.1103/PhysRevLett.129.101102>.

²For example, the AMS-02 data are not recommended to be shown in log-log format, they deserve the log-linear scale (Prof. Samuel Ting, personal communication, 2014).

- org/doi/10.1103/PhysRevLett.129.101102. doi:10.1103/PhysRevLett.129.101102.
- Adriani, O., Akaïke, Y., Asano, K. et al. (2021). Measurement of the iron spectrum in cosmic rays from 10 GeV/n to 2.0 TeV/n with the Calorimetric Electron Telescope on the International Space Station. *Phys. Rev. Lett.*, *126*(24), 241101. doi:10.1103/PhysRevLett.126.241101. arXiv:2106.08036.
- Adriani, O., Barbarino, G. C., Bazilevska, G. A. et al. (2011). PAMELA measurements of cosmic-ray proton and helium spectra. *Science*, *332*(6025), 69. doi:10.1126/science.1199172. arXiv:1103.4055.
- Aguilar, M., Aisa, D., Alpat, B. et al. (2015). Precision measurement of the proton flux in primary cosmic rays from rigidity 1 GV to 1.8 TV with the Alpha Magnetic Spectrometer on the International Space Station. *Phys. Rev. Lett.*, *114*(17), 171103. doi:10.1103/PhysRevLett.114.171103.
- Aguilar, M., Ali Cavazonza, L., Ambrosi, G. et al. (2021a). The Alpha Magnetic Spectrometer (AMS) on the International Space Station: Part II – results from the first seven years. *Phys. Rep.*, *894*, 1–116. doi:10.1016/j.physrep.2020.09.003.
- Aguilar, M., Cavazonza, L. A., Allen, M. S. et al. (2021b). Properties of iron primary cosmic rays: Results from the Alpha Magnetic Spectrometer. *Phys. Rev. Lett.*, *126*(4), 041104. doi:10.1103/PhysRevLett.126.041104.
- Ahn, H. S., Allison, P., Bagliesi, M. G. et al. (2009). Energy spectra of cosmic-ray nuclei at high energies. *Astrophys. J.*, *707*(1), 593–603. doi:10.1088/0004-637X/707/1/593. arXiv:0911.1889.
- Alemanno, F., An, Q., Azzarello, P. et al. (2021). Measurement of the cosmic ray helium energy spectrum from 70 GeV to 80 TeV with the DAMPE space mission. *Phys. Rev. Lett.*, *126*(20), 201102. doi:10.1103/PhysRevLett.126.201102. arXiv:2105.09073.
- Amenomori, M., Bi, X. J., Chen, D. et al. (2017). Northern sky galactic cosmic ray anisotropy between 10 and 1000 TeV with the Tibet Air Shower Array. *Astrophys. J.*, *836*(2), 153. doi:10.3847/1538-4357/836/2/153. arXiv:1701.07144.
- An, Q., Asfandiyarov, R., Azzarello, P. et al. (2019). Measurement of the cosmic ray proton spectrum from 40 GeV to 100 TeV with the DAMPE satellite. *Sci. Adv.*, *5*(9). URL: <https://www.science.org/doi/10.1126/sciadv.aax3793>. doi:10.1126/sciadv.aax3793.
- Becker Tjus, J., & Merten, L. (2020). Closing in on the origin of Galactic cosmic rays using multimessenger information. *Phys. Rep.*, *872*, 1–98. doi:10.1016/j.physrep.2020.05.002. arXiv:2002.00964.
- Blandford, R. D., & Ostriker, J. P. (1978). Particle acceleration by astrophysical shocks. *Astrophys. J. Lett.*, *221*, L29–L32. doi:10.1086/182658.
- Blasi, P., Amato, E., Aloisio, R. et al. (2022). A modern approach to cosmic ray transport in the Galaxy. *Mem. S.A.I.*, *93*(2-3), 168. doi:10.36116/MEMSAIT-93N2-3.2022.22.
- Boschini, M. J., Della Torre, S., Gervasi, M. et al. (2020). Inference of the local interstellar spectra of cosmic-ray nuclei $Z \leq 28$ with the GALPROP-HELMOD framework. *Astrophys. J. Suppl.*, *250*(2), 27. doi:10.3847/1538-4365/aba901. arXiv:2006.01337.
- Boschini, M. J., Della Torre, S., Gervasi, M. et al. (2021). The discovery of a low-energy excess in cosmic-ray iron: Evidence of the past supernova activity in the Local Bubble. *Astrophys. J.*, *913*(1), 5. doi:10.3847/1538-4357/abf11c. arXiv:2101.12735.
- Burlaga, L. F., Ness, N. F., Berdichevsky, D. B. et al. (2019). Magnetic field and particle measurements made by Voyager 2 at and near the heliopause. *Nature Astronomy*, *3*, 1007–1012. doi:10.1038/s41550-019-0920-y.
- Chakraborty, M., Ahmad, S., Chandra, A. et al. (2023). Small-scale cosmic ray anisotropy observed by the GRAPES-3 experiment at TeV energies. arXiv:2310.15489.
- Chen, C. H. K., Bale, S. D., Bonnell, J. W. et al. (2020). The evolution and role of solar wind turbulence in the inner heliosphere. *Astrophys. J. Suppl.*, *246*(2), 53. URL: <https://doi.org/10.3847/1538-4365/ab60a3>. doi:10.3847/1538-4365/ab60a3.
- Chernyshov, D. O., Dogiel, V. A., Ivlev, A. V. et al. (2022). Formation of the cosmic-ray halo: The role of nonlinear Landau damping. *Astrophys. J.*, *937*(2), 107. doi:10.3847/1538-4357/ac8f42. arXiv:2209.12302.
- Chernyshov, D. O., Ivlev, A. V., & Dogiel, V. A. (2023). Secondary cosmic-ray nuclei in the model of Galactic halo with nonlinear Landau damping. arXiv e-prints, (p. arXiv:2309.04772). doi:10.48550/arXiv.2309.04772.
- arXiv:2309.04772.
- Choi, G., Seo, E., Aggarwal, S. et al. (2022). Measurement of high-energy cosmic-ray proton spectrum from the ISS-CREAM experiment. *Astrophys. J.*, *940*(2), 107.
- Gabici, S. (2023). Rapporteur Talk: CRD. In *Proceedings of 38th International Cosmic Ray Conference — PoS(ICRC2023)* (p. 030). volume 444. doi:10.22323/1.444.0030.
- Gaia Collaboration (2020). VizieR Online Data Catalog: Gaia EDR3 (Gaia Collaboration, 2020). *VizieR Online Data Catalog*, (p. I/350).
- Grebnyuk, V., Karmanov, D., Kovalev, I. et al. (2019). Energy spectra of abundant cosmic-ray nuclei in the NUCLEON experiment. *Advances in Space Research*, *64*(12), 2546–2558. doi:10.1016/j.asr.2019.10.004.
- Karmanov, D., Kovalev, I., Kudryashov, I. et al. (2020a). Spectra of cosmic ray carbon and oxygen nuclei according to the NUCLEON experiment. *Physics Letters B*, *811*, 135851. doi:10.1016/j.physletb.2020.135851.
- Karmanov, D. E., Kovalev, I. M., Kudryashov, I. A. et al. (2020b). Spectra of protons and alpha particles and their comparison in the NUCLEON experiment data. *Soviet Journal of Experimental and Theoretical Physics Letters*, *111*(7), 363–367. doi:10.1134/S002136402007005X.
- Kulsrud, R., & Pearce, W. P. (1969). The effect of wave-particle interactions on the propagation of cosmic rays. *Astrophys. J.*, *156*, 445–469. doi:10.1086/149981.
- Lallement, R., Quémerais, E., Bertaux, J.-L. et al. (2005). Deflection of the interstellar neutral hydrogen flow across the heliospheric interface. *Science*, *307*(5714), 1447–1449.
- Lee, M. A., & Völk, H. J. (1973). Damping and non-linear wave-particle interactions of Alfvén-waves in the solar wind. *Astroph. and Space Sci.*, *24*(1), 31–49. doi:10.1007/BF00648673.
- Malkov, M. A. (2017). Exact solution of the Fokker-Planck equation for isotropic scattering. *Phys. Rev. D*, *95*(2), 023007.
- Malkov, M. A., Diamond, P. H., Sagdeev, R. Z. et al. (2013). Analytic solution for self-regulated collective escape of cosmic rays from their acceleration sites. *Astrophys. J.*, *768*, 73. doi:10.1088/0004-637X/768/1/73. arXiv:1207.4728.
- Malkov, M. A., & Moskalenko, I. V. (2021). The TeV cosmic-ray bump: A message from the Epsilon Indi or Epsilon Eridani star? (Paper I). *Astrophys. J.*, *911*(2), 151. URL: <https://doi.org/10.3847/1538-4357/abe855>. doi:10.3847/1538-4357/abe855.
- Malkov, M. A., & Moskalenko, I. V. (2022). On the origin of observed cosmic-ray spectrum below 100 TV (Paper II). *Astrophys. J.*, *933*(1), 78. doi:10.3847/1538-4357/ac7049. arXiv:2105.04630.
- Panov, A. D., Adams, J. H., Ahn, H. S. et al. (2009). Energy spectra of abundant nuclei of primary cosmic rays from the data of ATIC-2 experiment: Final results. *Bull. Russian Acad. Sci., Physics*, *73*(5), 564–567. doi:10.3103/S1062873809050098. arXiv:1101.3246.
- Qiao, B.-Q., Guo, Y.-Q., Liu, W. et al. (2023). Nearby SNR: a possible common origin of multi-messenger anomalies in the spectra, ratios, and anisotropy of cosmic rays. *Astrophys. J.*, *956*(2), 75. doi:10.3847/1538-4357/acf453. arXiv:2212.05641.
- Riley, A. H., Strigari, L. E., Porter, T. A. et al. (2019). Possible detection of gamma-rays from Epsilon Eridani. *Astrophys. J.*, *878*(1), 8. doi:10.3847/1538-4357/ab1a3c. arXiv:1810.04194.
- Sagdeev, R. Z., & Galeev, A. A. (1969). *Nonlinear Plasma Theory*. W.A. Benjamin Inc. New York, New York.
- Skilling, J. (1975a). Cosmic ray streaming. I - Effect of Alfvén waves on particles. *Mon. Not. R. Astron. Soc.*, *172*, 557–566.
- Skilling, J. (1975b). Cosmic ray streaming. III - Self-consistent solutions. *Mon. Not. R. Astron. Soc.*, *173*, 255–269.
- Swaczyna, P., Schwadron, N. A., Möbius, E. et al. (2022). Mixing interstellar clouds surrounding the Sun. *Astrophys. J. Lett.*, *937*(2), L32.
- Vladimirov, A. E., Jóhannesson, G., Moskalenko, I. V. et al. (2012). Testing the origin of high-energy cosmic rays. *Astrophys. J.*, *752*, 68. doi:10.1088/0004-637X/752/1/68. arXiv:1108.1023.
- Wood, B. E., Müller, H.-R., Zank, G. P. et al. (2002). Measured mass-loss rates of solar-like stars as a function of age and activity. *Astrophys. J.*, *574*(1), 412.
- Yoon, Y. S., Anderson, T., Barrau, A. et al. (2017). Proton and helium spectra from the CREAM-III flight. *Astrophys. J.*, *839*(1), 5. doi:10.3847/1538-4357/aa68e4. arXiv:1704.02512.
- Zhang, R., Huang, X., Xu, Z.-H. et al. (2023). Galactic diffuse γ -ray emission

from GeV to PeV energies in light of up-to-date cosmic-ray measurements.
arXiv:2305.06948.

Zhao, B., Liu, W., Yuan, Q. et al. (2022). Geminga snr: Possible candidate of the local cosmic-ray factory. *The Astrophysical Journal*, 926(1), 41. URL: <https://dx.doi.org/10.3847/1538-4357/ac4416>. doi:10.3847/1538-4357/ac4416.